INTERNATIONAL JOURNAL OF NUMERICAL METHODS IN FLUIDS, VOL. 21, 467–488 (1995)

ANALYSIS OF UNSTEADY WAVE PROCESSES IN A ROTATING CHANNEL

L. M. LAROSILIERE

Ohio Aerospace Institute, Brook Park, OH 44142, U.S.A.

AND

M. MAWID

Engineering Research and Analysis (ERA), Skokie, IL 60077, U.S.A.

SUMMARY

The impact of passage rotation on the gasdynamic wave processes is analyzed through a numerical simulation of ideal shock-tube flow in a closed rotating-channel containing a gas in an initial state of homentropic solid-body rotation. Relevant parameters of the problem such as wheel Mach number, hub-to-tip radius ratio, length-to-tip radius ratio, diaphragm temperature ratio, and diaphragm pressure ratio are varied. It is shown that for a fixed geometry and initial conditions, the contact interface acquires a distorted three-dimensional time-dependent orientation at non-zero wheel Mach numbers. At a fixed wheel Mach number, the level of distortion depends primarily on the density ratio across the interface and also the hub-to-tip radius ratio. The nature of the rarefaction and shock wave propagation is one-dimensional, although the acoustic waves are diffracted due to the radially varying propagation speed. Under conditions of initially homentropic solid-body rotation, a degree of similarity exists between rotating and stationary shock-tube flows. This similarity is exploited to arrive at an approximate analytical solution to the Riemann problem in a rotating shock-tube.

KEY WORDS: gas dynamics; wave rotor; shock-tube flow

INTRODUCTION

The goal of this paper is to analyse for shock tube flow the manner in which centripetal and Coriolis accelerations brought on by the rotation of a closed channel impact the wave processes. Wave processes considered are gasdynamic ones, including shock waves, contact interfaces and rarefaction waves but excluding deflagrations and detonations. Herein, shock tube flow is generated by the instantaneous rupture of a diaphragm separating a high-pressure gas from a lower-pressure gas of the same composition. Gasdynamic waves are initiated and propagated in a closed rotating channel containing a gas initially in a state of homentropic solid body rotation. Apart from general interest in unsteady compressible flow, understanding the propagation and interaction of gasdynamic waves in a rotating channel is useful for pressure exchange wave rotor[1] applications. For a wave rotor, predictions of wave propagation speeds as well as distortion of fluid contact interfaces are required for performance assessment.

The approach taken is to formulate the rotating shock tube problem in terms of the three-dimensional unsteady Euler equations in a rotating reference frame. Dimensionless variables are introduced, thereby allowing relevant parameters to be identified. The aim is to characterize the influence of these parameters on the wave processes. Although the primary concern is with the unsteady gasdynamics, the parameters of the problem are carefully varied in a range applicable to wave

CCC 0271–2091/95/060467–22

Received 3 January 1994
Revised 24 January 1995

rotor designs. To gain full insight into the wave processes in a rotating channel, an approximate analytical solution that neglects the vortical structure of the contact interface is also provided.

The one-dimensional theory of shock tube flow in a closed stationary channel is reviewed by Glass and Patterson.[2] A classical shock tube consists of a channel initially separated into two parts by a diaphragm. Both parts are filled with gas, which is permitted to settle to rest and a uniform state so that its temperature becomes uniform throughout the tube, but the pressures in the two parts are arranged to be different. When the diaphragm is instantaneously ruptured (in the ideal case), a wave system consisting of a shock followed by a fluid contact interface is transmitted into the low-pressure side of the channel and a centred rarefaction front propagates into the high-pressure side. This wave system can be represented in an (x, t) plane as shown in Figure 1. The left (L) and right (R) states are prescribed at time $t=0$ and the waves are illustrated with straight lines emanating from the origin. Note that the rarefaction fronts consists of a series of Mach lines along which flow quantities are constant but vary from line to line. State (2), which is compressed by the shock wave, and state (3), which is formed from the isentropic expansion of the gas in the high-pressure side through the rarefaction front, are uniform regions. The fluid velocity and the pressure in the two uniform states are identical. However, because of the different formative processes involved, the temperature, density and entropy of the two states are different. Therefore these two uniform states are separated by a contact interface. For a perfect gas the wave speeds and the properties of the uniform states are readily determined from the initial conditions.

For the case of a rotating shock tube the centripetal and Coriolis accelerations may disrupt the one-dimensionality of the classical shock tube flow. To the authors' knowledge, the question of exactly how the wave processes differ from the classical non-rotating shock tube for a given rotational speed has not been addressed in the open literature. The primary aim of this paper is to provide the correct framework in which to answer this question and to give specific analytic and numerical examples illustrating this framework.

This paper is organized as follows. In the next section the equations of motion written in a rotating reference frame are made dimensionless. This results in a clear identification of the relevant parameters of the problem. The question of similarity between stationary and rotating shock tube flow is then investigated. This investigation leads to an approximate solution for the Riemann problem in a rotating shock tube flow. In the following section, numerical solutions of the governing equations for various ranges of the problem parameters are presented and discussed. These results suggest criteria for estimating the extent to which passage rotation impacts the gasdynamic wave processes. Finally a summary of the major findings is given.

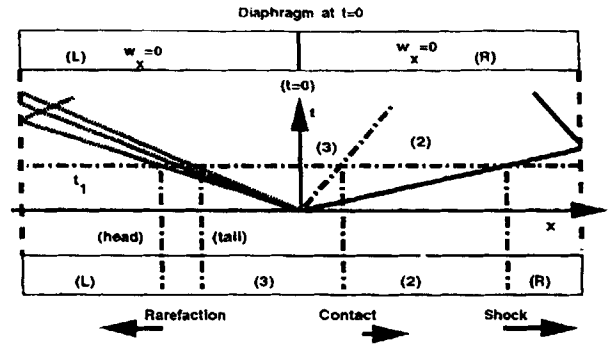

Figure 1. Theoretical x–t diagram of the wave system produced in a classical shock tube flow

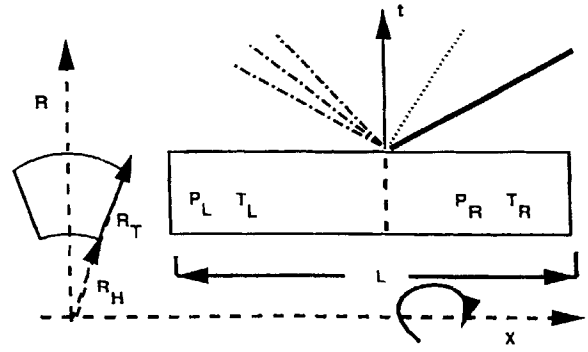

Figure 2. Rotating channel geometry illustrating the generation of a wave system by the instantaneous rupture of a diaphragm

FORMULATION

The geometric configuration chosen to illustrate the effects of passage rotation consists of a closed cylindrical channel (Figure 2) rotating about its length. Viscous and heat conduction contributions are neglected. This reduces the mathematical formulation to that of the Euler equations in a rotating reference frame.

The rotating shock tube problem involves a combination of the classic stationary shock tube flow in a closed channel and the homentropic flow of a fluid undergoing solid body rotation. Boundary and initial conditions for these two flows may be anticipated to define intrinsic scales of the problem. The flow is initiated by first imposing homentropic solid body rotation on the fluid on both sides of the diaphragm and then rupturing the diaphragm, thereby generating the wave system. Note that the uniform entropy of the gas is different on each side of the diaphragm. Of particular interest here is the orientation of the contact interface at specific positions along the length of the closed channel. Thus the relevant time scale is the time for waves to propagate axially along the channel. The tip radius is taken to be the length scale over which centrifugal effects are important, while the length of the channel is assumed to correspond to the wave propagation length scale.

Governing equations

Dimensionless variables are introduced in order to reduce the number of parameters that occur explicitly. Consistent with the problem at hand, the equations are made dimensionless by scaling with the channel length L for the axial dimension, the tip radius R_T for the radial dimension, a density ρ_∞, a speed of sound a_∞ and a reference time L/a_∞. The uniform thermodynamic reference state '∞' is that which would exist at the centre of rotation in the low-pressure side of the passage prior to rupturing the diaphragm if the height of the channel were to be extended to the centre of rotation.

Combinations of L, R_T, ρ_∞ and a_∞ are selected so that the following variables defined without asterisks are dimensionless:

$$x = \frac{x^*}{L}, \qquad t = \frac{t^*}{L/a_\infty}, \qquad \rho = \frac{\rho^*}{\rho_\infty}, \qquad \vec{w} = \frac{\vec{w}^*}{a_\infty}, \qquad p = \frac{p^*}{\rho_\infty a_\infty^2},$$

$$R = \frac{R^*}{R_T}, \qquad E = \frac{E^*}{a_\infty^2}, \qquad s = \frac{s^*}{\gamma R_g}, \qquad \vec{\nabla} = L\vec{\nabla}^*.$$

Let (R, x, θ) denote cylindrical co-ordinates attached to the rotating channel. The x-axis lies along the axis of rotation and the rotating channel is restricted by the six walls $\theta = 0$, $\theta = \Phi$, $R = R_H/R_T$, $R = 1$,

$x=0$ and $x=1$. The flow is modelled by the unsteady three-dimensional Euler equations[3] written in a rotating reference frame,

$$\frac{\partial \rho}{\partial t} + \vec{\nabla} \cdot (\rho \vec{w}) = 0, \tag{1a}$$

$$\frac{\partial \rho \vec{w}}{\partial t} + \vec{\nabla} \cdot (\rho \vec{w} \otimes \vec{w}) + 2R_\Omega \rho \hat{e}_\Omega \times \vec{w} - \rho M_\Omega^2 \vec{\nabla}\left(\frac{R^2}{2}\right) = -\vec{\nabla} p, \tag{1b}$$

$$\frac{\partial \rho E}{\partial t} + \vec{\nabla} \cdot (\rho \vec{w} h_{\mathrm{tR}}) = 0, \tag{1c}$$

completed by the perfect gas state relation

$$T = \gamma \frac{p}{\rho}, \tag{1d}$$

where h_{tR} is the rothalpy,

$$h_{\mathrm{tR}} = \frac{T}{\gamma - 1} + \tfrac{1}{2} w^2 - \tfrac{1}{2} M_\Omega^2 R^2, \tag{1e}$$

and E is the total energy per unit mass in the rotating frame,

$$E = h_{\mathrm{tR}} - \frac{p}{\rho}. \tag{1f}$$

The free slip wall velocity boundary conditions are

$$\vec{w} \cdot \hat{n} = 0 \quad \text{for} \begin{cases} R = 1, & R = R_{\mathrm{H}}/R_{\mathrm{T}}, \\ x = 0, & x = 1, \\ \theta = 0, & \theta = \Phi. \end{cases} \tag{1g}$$

The dimensionless parameter R_Ω is defined as

$$R_\Omega = \frac{L/a_\infty}{1/\Omega}.$$

This parameter is a measure of the ratio of the time scale of motion (i.e. transit time) to that of rotation. It should be noted that R_Ω scales only the Coriolis acceleration and is thus unimportant if this acceleration is not significant. Another dimensioness parameter is the wheel Mach number based on the tip rotational speed, defined as

$$M_\Omega = \frac{\Omega R_{\mathrm{T}}}{a_\infty}.$$

This is primarily a measure of the level of radial stratification established by the centripetal acceleration. Note that $R_\Omega = M_\Omega L/R_{\mathrm{T}}$ and the parameter L/R_{T} is also implicitly contained in the gradient operator.

The governing equations and boundary conditions clearly show that the relevant parameters of the problem to be the wheel Mach number M_Ω, the length-to-tip radius ratio L/R_{T}, the hub-to-tip radius ratio $R_{\mathrm{H}}/R_{\mathrm{T}}$, the passage sector angle Φ and the initial conditions.

Initial conditions

Steady homentropic ($\vec{\nabla} s = 0$) solid body rotation ($\vec{w} = 0$) is assumed to exist on both sides of the diaphragm prior to it being ruptured. Note that the entropy differs on each side of the diaphragm.

Under these conditions and using the Gibbs relation

$$T\vec{\nabla}s = \frac{\vec{\nabla}T}{\gamma - 1} - \frac{\vec{\nabla}p}{\rho}, \tag{2}$$

the equations of motion can be manipulated (see Reference 3 for details) to obtain

$$\vec{\nabla}h_{tR} = 0.$$

Thus the rothalpy is uniform throughout each side of the diaphragm. The initial states on each side of the diaphragm may be obtained

$$T_0(R) = T_C + \frac{\gamma - 1}{2} M_\Omega^2 (R^2 - R_C^2), \tag{3a}$$

$$P_0(R) = P_C \left(\frac{T_0}{T_C}\right)^{\gamma/(\gamma-1)}, \tag{3b}$$

$$\rho_0(R) = \gamma \frac{P_0}{T_0}, \tag{3c}$$

where P_C and T_C are the pressure and temperature (i.e. P_L, T_L, P_R, T_R) at the reference radius R_C. For the present study and also for the sake of simplicity, R_C is taken as the centre of rotation ($R_C = 0$) on each side of the diaphragm.

Similarity

We now investigate the similarities between the rotating shock tube flow and the classical stationary shock tube. Consider an arbitrary surface moving in the flow region with a certain normal velocity $v_s\vec{n}$ relative to the fluid particles instantaneously situated on it. The orientation of the surface is specified at any point by the unit normal vector. A natural local co-ordinate system is imagined, based on any intrinsic two-dimensional co-ordinate system on the surface. It can be shown that[4]

$$\frac{d\vec{n}}{dt} = \vec{\omega}_s \times \hat{n} = -\vec{\nabla}_t v_s, \tag{4}$$

where

$$\frac{d}{dt} = \frac{\partial}{\partial t} + v_s \frac{\partial}{\partial n}$$

is the total rate of change taken at a point lying on the surface and also moving in a direction normal to the surface. The vector $\vec{\omega}_s$ is the tangential part of the local angular velocity of the surface and the subscript 't' on the gradient operator indicates that only the tangential part of the derivative (i.e. derivatives along the surface) is included. Note that equation (4) is a strictly kinematic relation without any consideration for the dynamics or thermodynamics of the processes involved in the creation of the surface. Hence it may be applied to determine the orientation of the shock, rarefaction fronts and contact interface once the local propagation speed of these surfaces is known.

The rarefaction region consists of a series of surfaces each carrying a discontinuity in the pressure gradient and moving with the local speed of sound (i.e. Mach wave with $v_s = \pm a$). There are no jumps in the entropy gradient or the relative vorticity $\vec{\omega}_R = \vec{\nabla} \times \vec{w}$ across these surfaces.[5] This implies that if the flow in the rarefaction region is initially homentropic and undergoing solid body rotation, it will

remain so. In addition, the wall boundary conditions require that

$$\vec{w} = w_x(x, t)\hat{e}_x.$$

Under these circumstances the Gibbs relation (2) and the equations of motion (1a–f) can be used to obtain governing equations valid in the rarefaction region:

$$\frac{\partial \rho}{\partial t} + \frac{\partial \rho w_x}{\partial x} = 0, \tag{5a}$$

$$\frac{\partial w_x}{\partial t} + \frac{\partial h_{\mathrm{tR}}}{\partial x} = 0, \tag{5b}$$

$$\frac{\partial h_{\mathrm{tR}}}{\partial R} = \frac{\partial h_{\mathrm{tR}}}{\partial \theta} = 0. \tag{5c}$$

Equation (5c) implies that the rothalpy is circumferentially and radially uniform. The above equations are similar to the governing equations for the non-rotating case with the rothalpy being the analogue of the total enthalpy. These equations (5a–c) can be manipulated to obtain

$$\frac{\partial J^{\pm}}{\partial t} + (w_x \pm a)\frac{\partial J^{\pm}}{\partial x} = 0, \tag{6a}$$

$$\pm a \frac{\partial J^{\pm}}{\partial R} = M_{\Omega}^2 R, \tag{6b}$$

where J is the Riemann variable defined as

$$J^{\pm} = w_x \pm \frac{2a}{\gamma - 1}.$$

The solutions of equation (6a) correspond to the propagation of waves, but these differ from the non-rotating case in that a radial equilibrium condition, equation (6b), has to be satisfied always. Consider a J^{-} wave travelling at a constant radius; according to equation (6), this wave will propagate longitudinally at the local speed of sound relative to the fluid particles instantaneously situated on it. As the wave arrives at an axial position, its arrival is communicated to the other radial locations through a radial equilibrium constraint. Furthermore, since the speed of sound varies radially, equation (4) implies that the sonic surfaces or Mach waves will not be radial but inclined at an angle depending on the wheel Mach number and the direction of propagation.

The shock wave is a surface of discontinuity in the Euler limit and is governed by the Rankine–Hugoniot jump relations.[5] These relations supply a complete set of boundary conditions at the surface of the shock. For a shock there is no jump in the velocity components tangent to the shock surface. This implies that if the flow ahead of the shock is in solid body rotation, the flow behind the shock will have no relative velocity components tangent to the shock surface. Consequently, because of the wall boundary conditions ($\vec{w} \cdot \hat{n} = 0$) and the initial conditions ($\vec{w} = 0$), the surface of the shock will be normal to the axial velocity component ($\hat{n} = \hat{e}_x$). This leads to a uniform shock propagation speed as can be seen from equation (4) with the condition $\mathrm{d}\hat{n}/\mathrm{d}t = 0$. Thus no vorticity will be generated at the shock and the flow immediately behind the shock will be in solid body rotation. The rothalpy and axial velocity immediately behind the shock are thus uniform.

The contact interface is also a surface of discontinuity satisfying the Rankine–Hugoniot jump conditions in the Euler limit. Across the interface there is no jump in the velocity component normal to the surface of the interface and also the pressure is continuous. However, the density and tangential velocity may jump by any amount. There is a density gradient at the interface that will combine with

the radial pressure gradient due to centripetal acceleration to produce vorticity according to[5]

$$\frac{\partial}{\partial t}\left(\frac{\vec{\omega}_R}{\rho}\right) + \vec{w}\cdot\vec{\nabla}\left(\frac{\vec{\omega}_R}{\rho}\right) = \frac{\vec{\omega}_R}{\rho}\cdot\vec{\nabla}\vec{w} - \frac{1}{\rho}\left(R_\Omega\vec{\nabla}\times(\hat{e}_\Omega\times\vec{w}) - \frac{1}{\rho^2}\vec{\nabla}\rho\times\vec{\nabla}p\right). \tag{7}$$

This vorticity and the ensuing Coriolis acceleration imply a locally three-dimensional flow field near the contact interface. The orientation of the interface can be obtained from equation (4) as

$$\frac{d\hat{n}}{dt} = \tfrac{1}{2}[\hat{n}\times(\omega_R\times\hat{n})]\times\hat{n}. \tag{8}$$

It has been shown that the flow in the rarefaction region is analogous to that in the corresponding region of the non-rotating shock tube (equations (5a– c)). Furthermore, the shock wave is normal to the flow and propagates with a uniform speed. If the vorticity generation at the contact interface is neglected, then there exists similarity between the rotating shock tube flow and the stationary shock tube. Note also that for a diaphragm temperature ratio T_L/T_R of 1 : 1 at the centre of rotation the pressure and temperature ratios are radially uniform (equations (3)). Hence for $T_L/T_R = 1:1$ there exists dynamical similarity between the two flows. Dynamical similarity implies that the local Mach numbers in corresponding regions of the flow are equivalent. Thus an approximate solution neglecting the vorticity generation at the interface can be obtained for the rotating shock tube problem under the aforementioned conditions by solving the one-dimensional stationary shock tube problem at the tip and hub radii and relating these two solutions through the constraint of radially uniform axial velocity and rothalpy. An outline of the solution procedure follows.

1. Given the diaphragm pressure and temperature ratios (i.e. $P_L P_R$, T_L/T_R), the wheel Mach number and the hub–tip ratio, set up initial conditions at the hub and tip radii using equations (3).
2. Solve the 1D Riemann problem for non-rotating shock tube flow at the hub and tip radii using standard techniques (see e.g. Reference 2).
3. Set the shock speed as the maximum of that obtained in step 2 at the hub and tip.
4. If the shock speed from step 3 corresponds to that obtained in step 2 at the tip, then set the axial velocity between the shock and the rarefaction to the corresponding value obtained in step 2. Also, set the rothalpy between the shock and the contact based on the tip radius. Otherwise set everything based on the hub radius.
5. The propagation speed of the head of the rarefaction front is set to that at the tip radius, while the speed of the tail is set to the axial velocity from step 4 minus the sonic speed for the corresponding region at the hub as obtained in step 2.
6. Set the rothalpy between the tail of the rarefaction front and the contract interface equal to a value calculated based on the corresponding hub temperature in step 2 and the axial velocity from step 4.
7. Isentropic relations along with equations (6) can be used to obtain properties across the rarefaction region.

The above procedure mimics the character of the processes in the different regions of the shock tube flow. It should be noted that the details of the radial adjustment across the rarefaction region are unaccountable in this approach, since in step 7 above the interactions of the expansion fans at the various radial sections are ignored. The error produced by neglecting the vorticity generation at the interface should be small for short times prior to any interaction of the interface with reflected waves. Thus there exists similarity with the stationary shock tube under conditions of radially and circumferentially uniform axial velocity, rothalpy and entropy. These conditions are approximately satisfied shortly after rupturing the diaphragm. Once the regions of the shock tube flow have been delineated as outlined above, a complete solution for the rotating shock tube can be obtained by invoking similarity. Approximate solutions obtained by this procedure are compared herein with the

computational results obtained by integrating the full three-dimensional Euler equations. This comparison should aid in understanding the results.

Computational scheme

For this investigation a two-stage Runge–Kutta scheme developed by Chima and Yokota[6] was applied to solve the Euler equations. This scheme uses explicit time marching along with central difference spatial discretization in a boundary-fitted H-mesh. Gasdynamic discontinuities (i.e. shocks and interfaces) are treated by means of a second-difference artificial dissipation. This implies that the Rankine–Hugoniot jumps associated with a shock or interface are continuous and spread out over a number of grid points rather than occurring as discontinuities. The dissipation coefficient was chosen so that the shock thickness is about five grid points independently of mesh size. A small amount of fourth-difference artificial dissipation is also employed to suppress non-linear instabilities. The formal truncation error of this scheme is second-order in space and first-order in time. Although the authors are well aware of the shortcomings of the present scheme relative to modern high-resolution schemes, it is believed that a well-calibrated artificial dissipation scheme will perform adequately for the range of parameters to be investigated.

To assess the accuracy and fidelity of the simulation, a zero-rotation case was run as a baseline for comparison. This is a one-dimensional problem with an exact analytical solution. A Courant number of one-half (CFL = 0·5) along with calibrated artifical dissipation parameters was selected. Initial conditions consisted of pressure and density ratios of 2 : 1 separating left and right states. Good

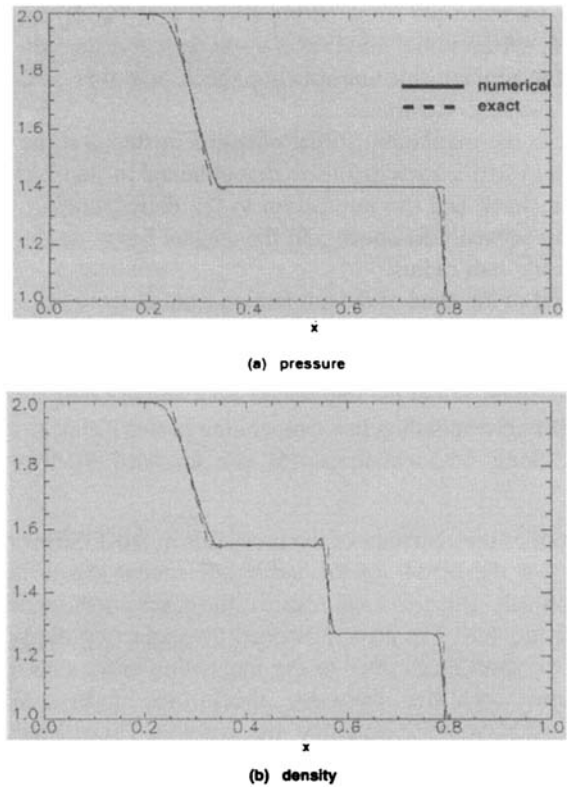

Figure 3. Comparison of numerical and exact solutions to the Riemann problem for shock tube flow. The density and pressure ratios are 2 : 1 and the time is $t = 0{\cdot}25$

comparison between the exact and computed solutions is shown in Figure 3. Based on these results, the required spatial and temporal resolutions were determined. A longitudinal spatial resolution of $\Delta x \leq 0{\cdot}0066$ was set. Further numerical experimentation demonstrated the ability of this scheme to adequately capture the essential features (i.e. wave speeds and interactions) pertinent to this investigation. The same numerical parameters were employed for all the cases presented.

RESULTS AND DISCUSSION

Five cases are presented to illustrate the impact of rotation on the wave processes for shock tube flow in a rotating passage. The parameters that are varied for each of the cases are given in Table I. The passage sector angle Φ was maintained at a constant value of 4·93° and the diaphragm was initially placed midway in the passage (i.e. $x = 0{\cdot}5$). These parameter ranges reflect possible operating conditions for proposed wave rotors being considered for thermodynamic cycle performance

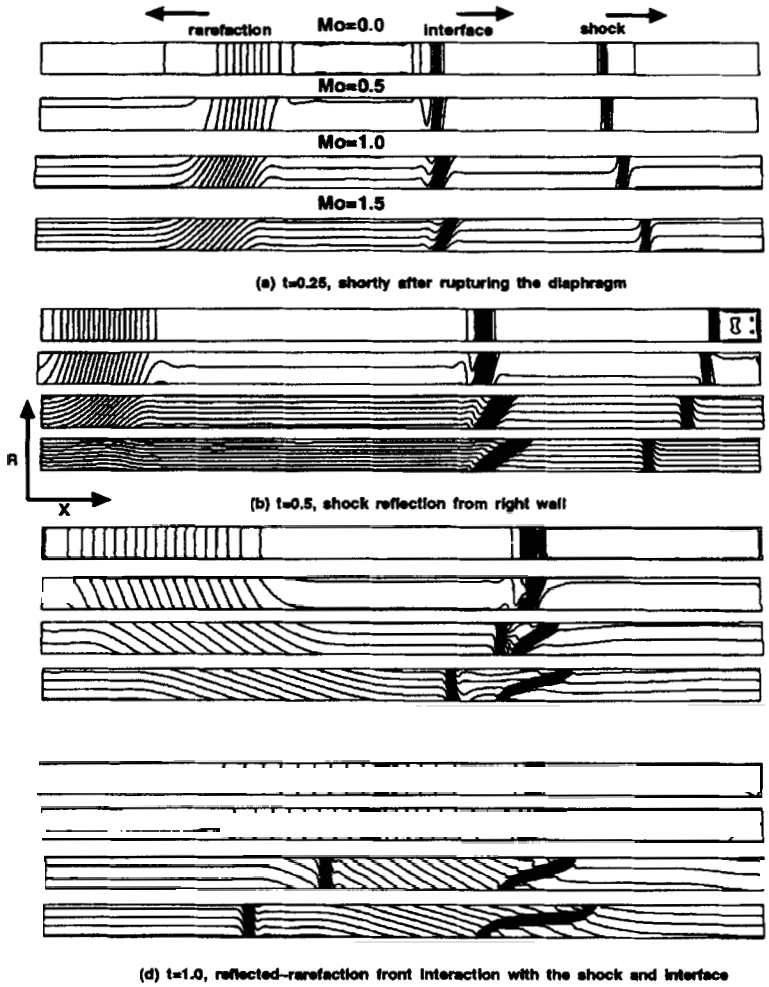

Figure 4. Four time sequences showing density contours in a meridional plane for various wheel Mach numbers and other parameters given in Table I for Case A. The pressure ratio is 2 : 1 and the temperature ratio is 1 : 1

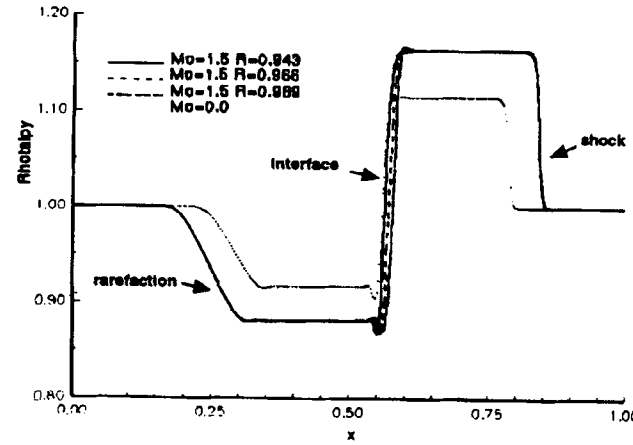

Figure 5. Axial variation in rothalpy and axial velocity at $t = 0{\cdot}25$ for wheel Mach numbers of 0·0 and 1·5 and other parameters pertaining to Case A. For $M_0 = 1{\cdot}5$ the hub, mean and tip profiles are also shown. The pressure ratio is 2 : 1 and the temperature ratio is 1 : 1

augmenttaion of small gas turbines. The computational mesh for all the cases consisted of 450 nodes in the x-direction, 20 nodes in the circumferential direction and 30 nodes in the radial direction, except Case E which had a size of 225 × 20 × 30. Increasing the number of mesh points in all three directions did not produce any significant differences in the results.

Table I. Parameters of rotating shock tube problem

Case	P_L/P_R	T_L/T_R	R_H/R_T	L/R_T	M_Ω, M_0
A. Rotational speed	2·0	1·0	0·934	1·5	0·0, 0·5, 1·0, 1·5
B. Pressure ratio	4·0, 2·0	1·0	0·934	1·5	0·5
C. Temperature ratio	2·0	0·5, 1·0, 2·0, 4·0	0·934	1·5	0·5
D. Hub–tip ratio	2·0	1·0, 4·0	0·5, 0·934	1·5	0·5
E. Length	2·0	1·0, 4·0	0·934	0·75, 1·5	0·5

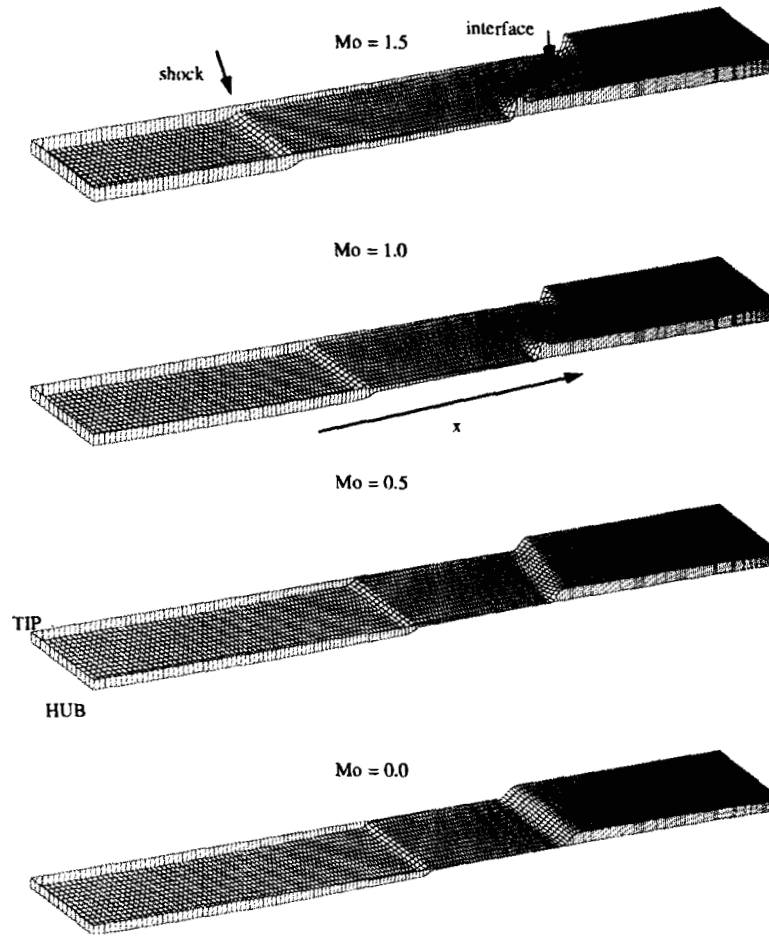

Figure 6. Meridional distribution of rothalpy in mid-passage at $t = 1{\cdot}0$ for various wheel Mach numbers. The pressure ratio is 2 : 1 and the temperature ratio is 1 : 1 (Case A)

Case A. Varying wheel Mach number

The effects of varying wheel Mach number on the density field are shown in Figure 4 for wheel Mach numbers of 0·0, 0·5, 1·0 and 1·5. For each wheel Mach number all other parameters are held constant as per Table I. Meridional ($\theta = \Phi/2$) projections of the shock, rarefaction fronts and interface are illustrated through density contours at four different moments in time.

Three observations follow from Figure 4. First, the shock, contact interface and rarefaction fronts travel faster with increasing wheel Mach number owing to the higher temperature consistent with the centrifugal force field and initial conditions. Second, for the zero wheel Mach number ($M_0 = 0$) the rarefaction fronts propagate along lines of radially constant density as in a centred expansion fan, whereas for non-zero wheel Mach numbers the constant density lines in the expansion fan are oblique, with the degree of obliquity varying in time as can be seen in a comparison of the $M_0 = 1{\cdot}0$ condition at $t = 0{\cdot}25$ and 0·5. This behaviour is compatible with equation (4) in that the sonic surface will tend to seek a shape having a uniform propagation speed along the surface (i.e. $\vec{\nabla}_t a = 0$). In addition, a normal

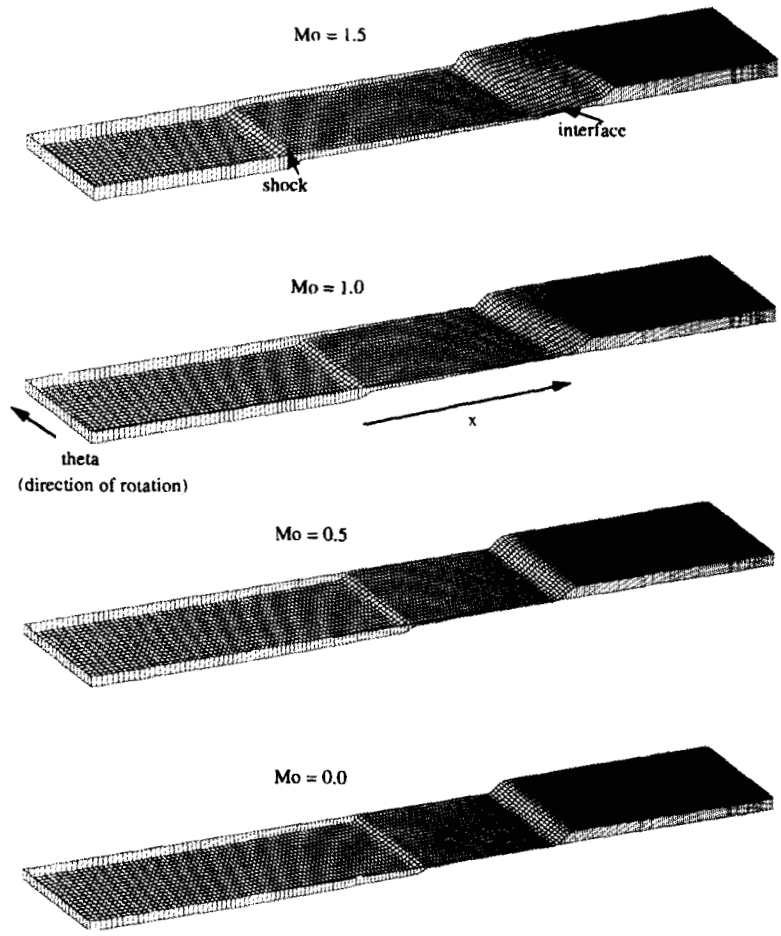

Figure 7. Rothalpy distribution in an axial–circumferential plane at mid-height for $t = 1{\cdot}0$. The pressure ratio is 2 : 1 and the temperature ratio is 1 : 1

shock with a uniform propagation speed is observed. Third, the largest departure from the non-rotating shock tube is the evolving distortion of the interface with increasing wheel Mach number. This is consistent with previous discussions concerning vorticity generation at the interface (equation (7)) and the evolution of the interface normal vector according to equation (8). The initiall radial interface becomes oblique before any interaction with the reflected shock or rarefaction fronts owing to the generation of baroclinic vorticity (i.e. $(\vec{\nabla}\rho/\rho) \times (\vec{\nabla}p/\rho)$. Interactions of the shock and rarefaction fronts with the interface result in stretching of the interface and at the same time the vorticity generation is amplified. For wheel Mach numbers greater than or equal to unity a rapidly growing non-planar orientation of the interface is observed after it interacts with the shock and rarefaction fronts. This can be better explained by considering the kinematics of stretching and alignment of fluid elements comprising the interface.[7] The evolution of a fluid element is determined by the local velocity gradient tensor, which includes a dilatation term (compression or expansion) and a rotational term (vorticity). The combination of these two actions and the wall boundary conditions is responsible for this interface orientation.

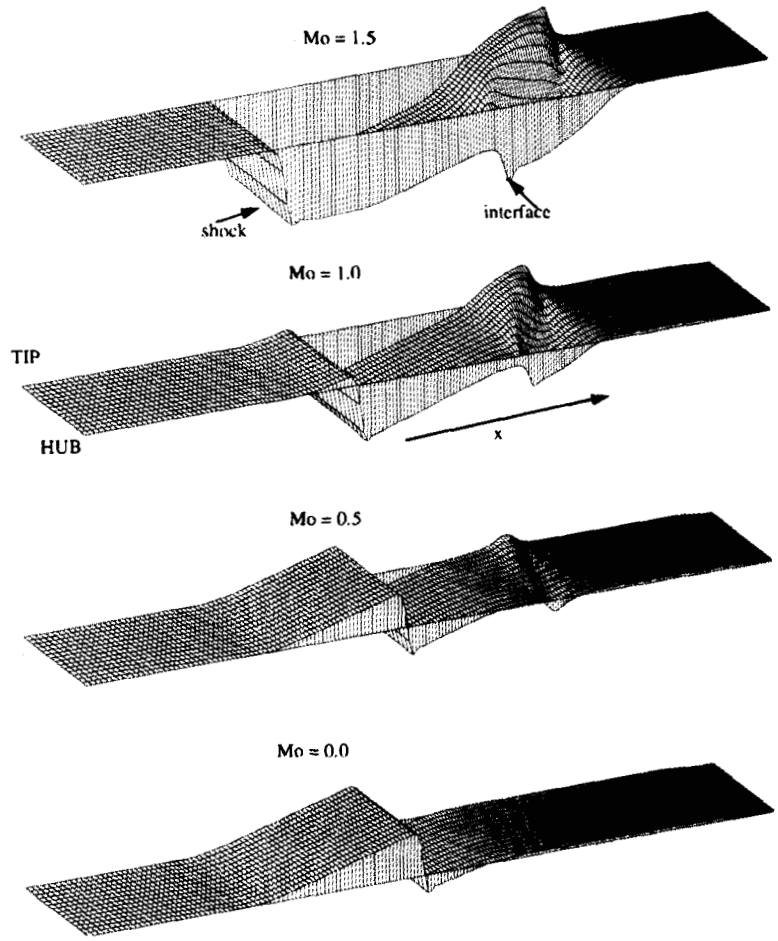

Figure 8. Meridional distribution of axial velocity at $t = 1.0$ for various wheel Mach numbers M_0 The pressure ratio is 2:1 and the temperature ratio is 1:1 (Case A)

A more quantitative illustration of the propagation of the shock and rarefaction fronts is shown in Figure 5. It can be seen that the rarefaction fronts appear to propagate in a one-dimensional fashion in terms of rothalpy and axial velocity fields. One says here 'appear to propagate' because the initial condition of homentropic solid body rotation constraints the rothalpy and axial velocity fields to be a function of only time and axial position away from the contact interface as previously discussed in the context of equations (5a–c). The increase in wave propagation speed as the wheel Mach number is increased from 0·0 to 1·5 is seen to be significant. This is due mainly to the initial conditions and may not have any significant implications for wave rotor applications.

The structure of the interface distortion is presented more clearly in Figure 6, where surface plots of the rothalpy distribution are shown in a meridional plane at mid-passage ($\theta = \Phi/2$) for the four wheel Mach numbers at $t = 1{\cdot}0$ after the reflected shock has interacted with the interface. It can be observed that the rothalpy is radially uniform except along the interface for non-zero wheel Mach numbers. An S-shaped fluid interface with an axially oriented mid-section appears to be developing for non-zero

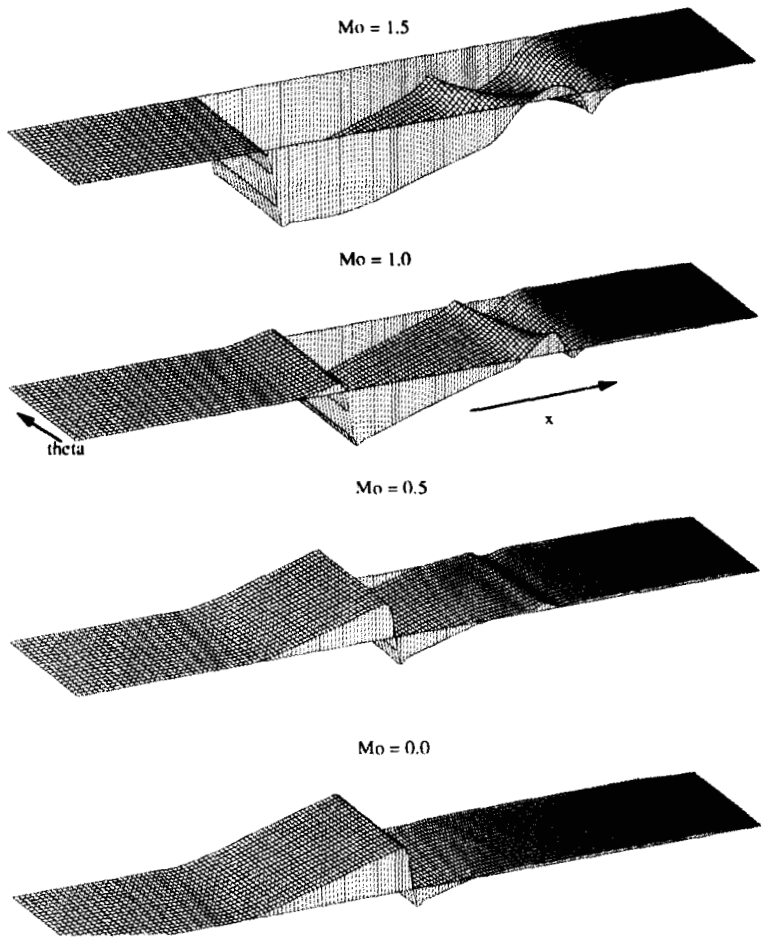

Figure 9. Axial velocity distribution in an axial–circumferential plane at mid-height for $t = 1{\cdot}0$. The pressure ratio is 2 : 1 and the temperature ratio is 1 : 1 (Case A)

wheel Mach numbers. The extent of the axially oriented mid-section increases with increasing wheel Mach number. Surface plots of the rothalpy distribution in an axial–circumferential plane at mid-height ($R = (1 + R_H/R_T)/2$ are shown in Figure 7 for $t = 1{\cdot}0$. The plots reveal the extent of interfacial distortion in this plane. In addition, for wheel Mach numbers of unity or above a noticeable non-planar orientation of the interface exists near the trailing side of the passage. The orientation of the interface is consistent with the vorticity production mechanisms and equation (8).

It appears that the interface seeks a 'stable' orientation when viewed in a meridional plane (Figures 4(d) and 6) as is exhibited for the $M_0 = 1{\cdot}5$ case. Stability here implies that the orientation of the interface is stationary to disturbances such as those caused by centripetal acceleration, Coriolis forces and interaction with waves.

To complete the general picture, axial velocity distributions in a meridional plane and an axial–circumferential plane are presented in Figures 8 and 9 respectively at $t = 1{\cdot}0$. A vortical structure is observed at the location of the interface for non-zero wheel Mach numbers. The orientation of the structure is consistent with that of the interface (Figures 6 and 7). A radially uniform axial velocity can be observed away from the interface. Thus the velocity field is one-dimensional everywhere except

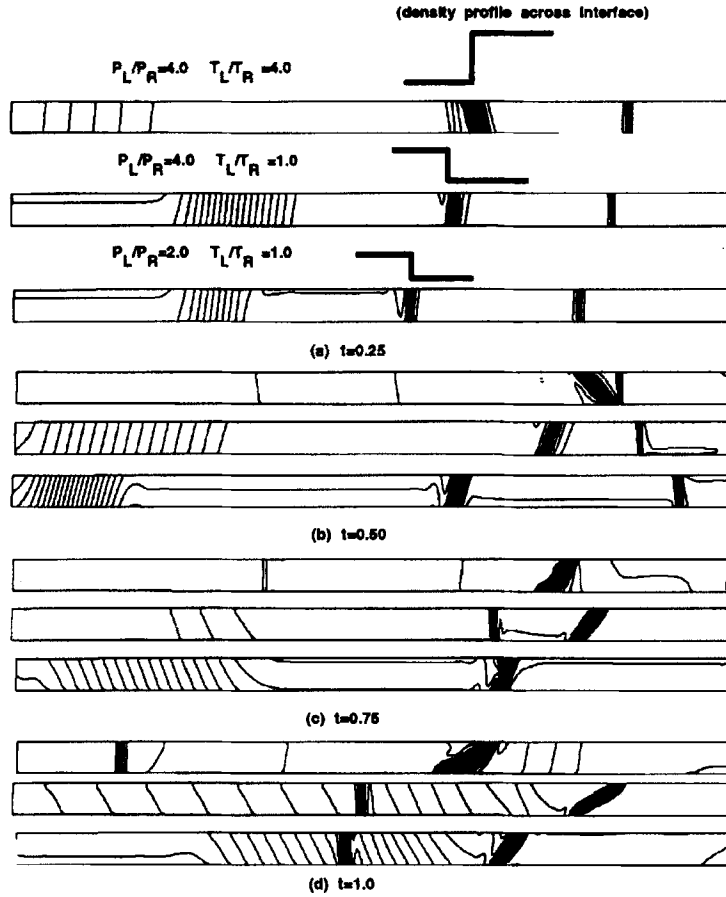

Figure 10. Density contours in a meridional plane for four time sequences illustrating the effect of varying diaphragm pressure ratio (Case B). The wheel Mach number is $M_0 = 0{\cdot}5$

near the interface, where the vortical structure induces tangential and radial velocities. These radial and tangential flows represent flow kinetic energy which is not available to the mean flow, so their kinetic energy must be considered a contribution to the inefficiency of the process.

Case B. Varying pressure ratio

Contour plots of the density field in a meridional plane are presented in Figure 10 at four time sequences for different diaphragm pressure ratios with all other parameters held constant as in Table I. An additional condition is shown for pressure and temperature ratios of 4·0 : 1 for comparison. Also included is a sketch of the density ratio across the interface shortly after rupturing the diaphragm. Increasing the diaphragm pressure ratio from 2·0 : 1 to 4·0 : 1 results in a relatively more distorted interface. For the temperature and pressure ratios of 4·0 : 1, although not definitively shown in the figures, the orientation of the interface changes direction after interaction with the reflected rarefaction fronts. Note also the deceleration of the shock wave at $t = 1{\cdot}0$ for $P_L/P_R = 4{\cdot}0$ and $T_L/T_R = 1{\cdot}0$ due to propagation in a region of higher fluid velocity.

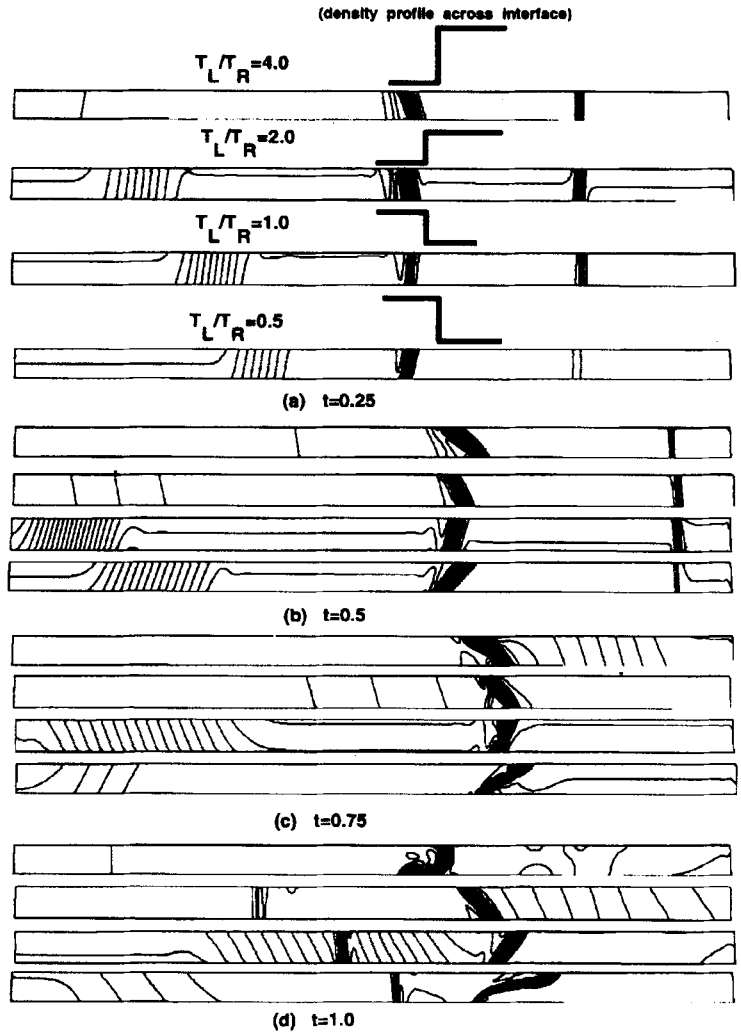

Figure 11. Density contours in a meridional plane for four time sequences illustrating the effect of varying diaphragm temperature ratio (Case C). The pressure ratio is 2 : 1 and $M_0 = 0{\cdot}5$

Case C. Varying temperature ratio

The effect of varying diaphragm temperature ratio at $M_0 = 0{\cdot}5$ is illustrated in Figure 11 through density contours in a meridional plane at various moments in time. Also indicated are the density ratios across the interface shortly after rupturing the diaphragm. It can be observed that for temperature ratios of 4·0 : 1 and 0·5 : 1 the interface is significantly distorted even before interaction with the reflected shock. Furthermore, for these same temperature ratios the interface orientation is very non-planar after interaction with the reflected shock ($t = 1{\cdot}0$). Thus large density ratios across the interface result in significant distortion of the interface.

Note also that for a temperature ratio of 4·0 : 1 the interface commences to roll over after interaction with the rarefaction fronts. This is probably caused by a non-uniform dilatation of the fluid elements along the interface. The exact roles of centripetal and Coriolis accelerations in sustaining this interface

configuration is not immediately apparent to the authors. In comparison with Case A (Figure 4) and the temperature ratio of 0·5 : 1, the orientation of the interface does not appear to be seeking a stable configuration for this temperature ratio of 4·0 : 1. It is apparent that for a range of temperature ratios above 1·0 the interface does not acquire a stable shape, whereas for temperature ratios of 1·0 or below the interface configuration becomes stable.

Case D. Varying L/R_T

Figures 12 and 13 illustrate the effect of reducing L/R_T through density contours in a meridional plane for two different temperature ratios. Recall that the longitudinal co-ordinates of the channels are dimensionless in these plots (i.e. $x = 0$–1). A better grid resolution was employed for the longer-length channel, which is why the discontinuities appear to be more smeared for the shorter length. Note that the reference time scale (L/a_∞) is different for these two configurations but the dimensionless times are the same. Thus this is a direct comparison of the effect of changing the residence time of a fluid element within the passage.

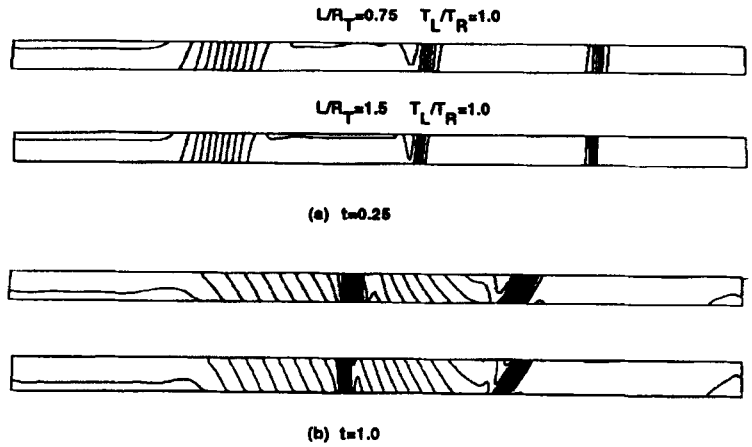

Figure 12. Effect of varying length-to-tip radius ratio for $T_L/T_R = 1{\cdot}0$ and $P_L/P_R = 2{\cdot}0$

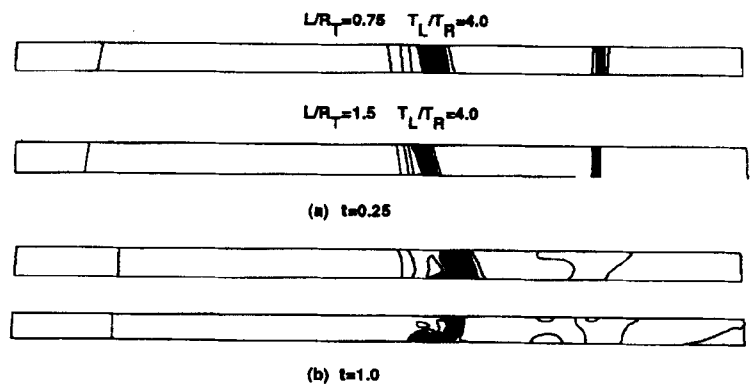

Figure 13. Effect of varying length-to-tip radius ratio for $T_L/T_R = 4{\cdot}0$ and $P_L/P_R = 2{\cdot}0$

Varying L/R_T at constant wheel Mach number changes $R_{\Omega,}$, which affects the Coriolis term in the equations of motion. Thus reducing L/R_T should lessen the degree of skewing of the interface as is evident in Figures 12 and 13. The effects of reducing L/R_T are more pronounced at the higher temperature ratio. Note that since the distortion of the interface is partly scaled by R_Ω, it may be possible to infer from Figure 13(b) the role of Coriolis forces in the stability of the interface. These results suggest that depending on the operating conditions, a shorter length may be better for an application where compressed fluid is drawn out at the end of the channel.

Case E. Varying hub–tip ratio

The effects of reducing R_H/R_T are shown in Figures 14 and 15. These figures display the meridional distribution of density for two different temperature ratios. It can be observed that increasing the hub–tip ratio generates a larger radial stratification, resulting in a non-planar orientation of the interface after interaction with the reflected shock. Varying the hub-to-tip radius ratio changes the stratification height, resulting in a radially non-uniform baroclinic vorticity generation. Note that for the higher temperature ratio the roll-over characteristic of the interface is not evident with the lower hub-to-tip ratio.

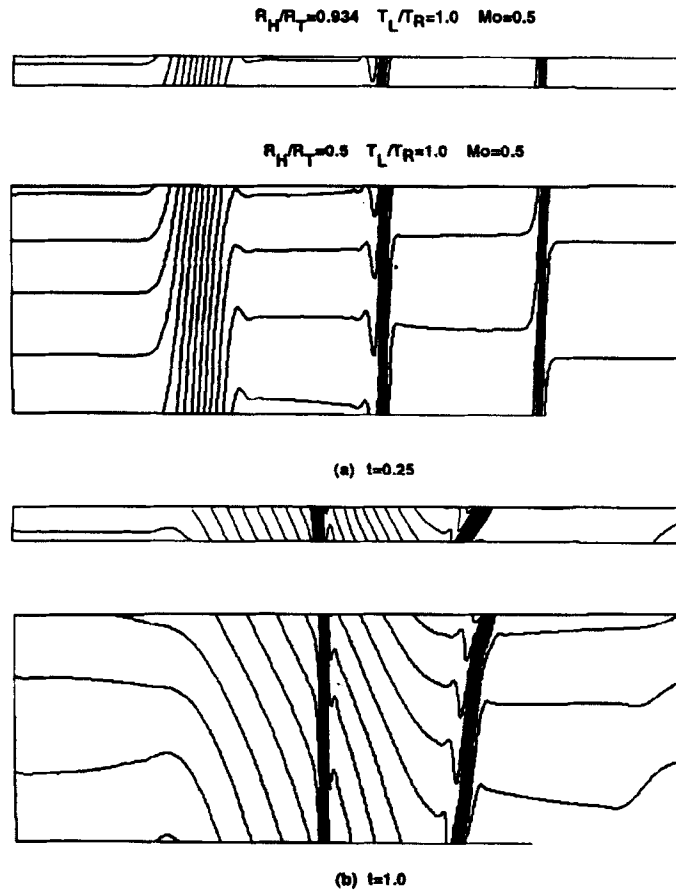

Figure 14. Effect of varying hub-to-tip radius ratio for $T_L/T_R = 1{\cdot}0$ and $P_L/P_R = 2{\cdot}0$

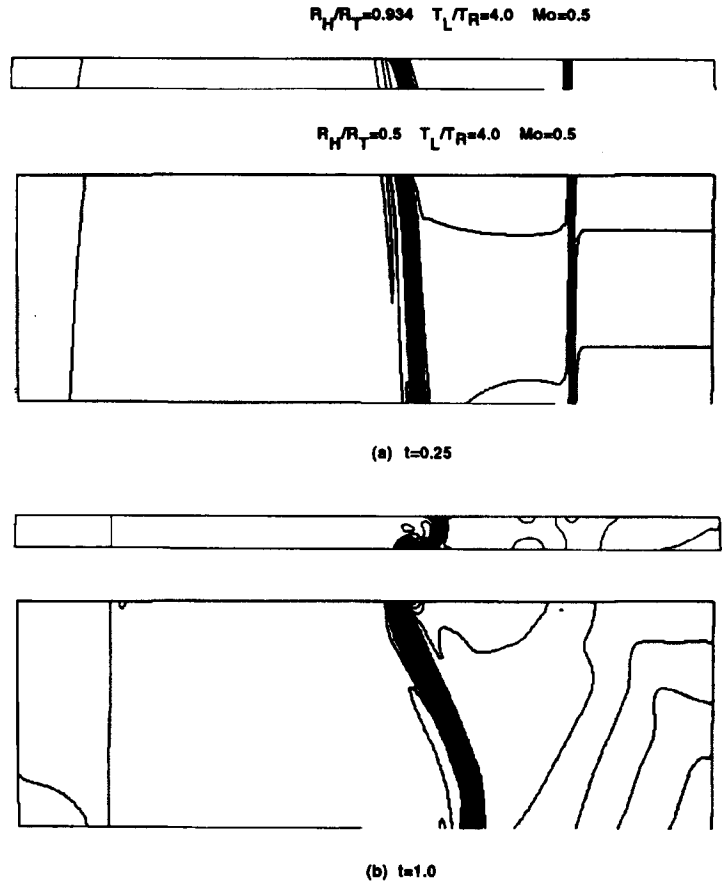

Figure 15. Effect of varying hub-to-tip radius ratio for $T_L/T_R = 4{\cdot}0$ and $P_L/P_R = 2{\cdot}0$

Comparisons with approximate analytical solution

Figure 16 compares some of the computational results with the approximate analytical solution previously outlined for a time $t = 0{\cdot}25$. This figure illustrates the axial variation in rothalpy and axial velocity at mid-height for various parameters. The stationary shock tube case ($M_0 = 0$) is included as a baseline. At a diaphragm temperature ratio of 4 : 1 there is a large overshoot in the computational results at the interface but the resolution of the interface is reasonably sharp. A good match with the analytical approximation is observed. This suggests that for an initially homentropic solid body rotation the character of the rarefaction and shock waves is not greatly altered by the passage rotation and can thus be approximately treated with techniques for one-dimensional stationary shock tube flow and the appropriate modifications discussed herein. To satisfy radial equilibrium, a radial adjustment of the thermodynamic properties must occur as the waves propagate along the channel.

CONCLUDING REMARKS

Some insights into the unsteady wave processes in a closed rotating channel are presented. Analysis of the governing equations revealed the dominant parameters controlling the problem. Three-dimensional

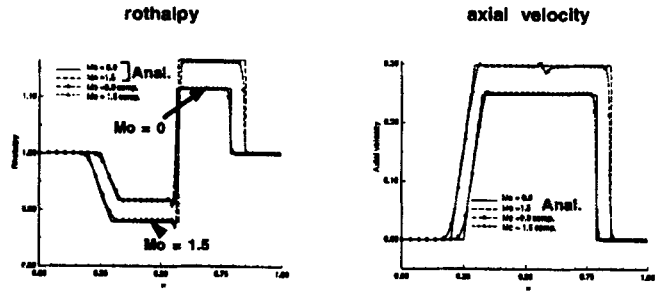

(a) Varying wheel Mach number for a pressure ratio of 2:1 and a temperature ratio of 1:1

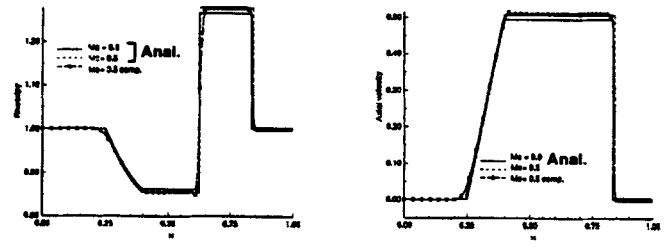

(b) Varying wheel Mach number for a pressure ratio of 4:1 and a temperature ratio of 1:1 .

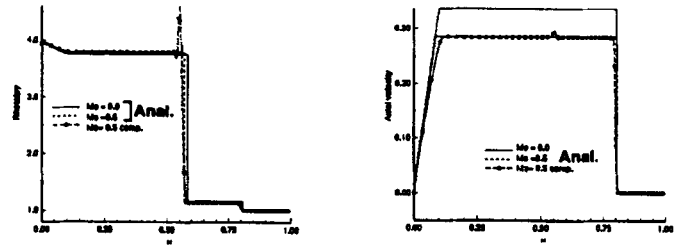

(c) Varying wheel Mach number for a pressure ratio of 2:1 and a temperature ratio of 4:1 .

Figure 16. Comparison of approximate analytical solution with computational (symbols) results at $t = 0{\cdot}25$

numerical results for ideal shock tube flow in a closed rotating channel show the influence of these parameters on the flow.

The following conclusions may be drawn concerning the impact of passage rotation on an ideal shock tube flow having initial conditions of homentropic solid body rotation on each side of the diaphragm.

1. Centripetal acceleration initiates baroclinic vorticity which creates Coriolis forces, resulting in a three-dimensional distortion of the fluid interface.
2. Subsequent interactions of the interface with shocks or rarefaction fronts dilate the interface and at the same time amplify the vorticity at the interface. For a range of diaphragm temperature ratios above 1·0 these interactions may result in an unstable interface configuration.
3. The magnitude of the distortion depends primarily upon the following parameters: the wheel Mach number M_Ω, the hub–tip radius ratio R_H/R_T and the density ratio across the interface.
4. For an application where compressed fluid is drawn out at the end of the channel, it may be

beneficial to reduce the length-to-tip radius ratio L/R_T of the channel so that the interface distortion due centripetal and Coriolis accelerations is minimized.

5. The shock is normal to the flow and propagates in a one-dimensional fashion. However, the rarefaction fronts also exhibit a one-dimensional propagation although the Mach waves are diffracted owing to the radially varying temperature.

For initial conditions other than those of homentropic solid body rotation the above conclusions may not hold exactly, i.e. the propagation of the shock and rarefaction fronts may acquire a three-dimensional character. It should also be noted that viscous effects were neglected and it is possible that they may have an appreciable impact on some of the conclusions drawn here.

ACKNOWLEDGEMENTS

We thank Dr. Larry Bober, Chief of Turbomachinery Technology at NASA LeRC, for suggesting this investigation. We also thank our colleagues Fred Newman and Gerard Welch for many useful discussions and valuable suggestions.

APPENDIX: NOMENCLATURE

a	speed of sound
$\hat{e}$	unit vector
E	total energy per unit mass
h_{IR}	rothalpy
L	passage length
M_o, M_Ω	wheel Mach number based on tip radius and a reference speed of sound
$\hat{n}$	unit normal vector
p	pressure
R_g	gas constant
R_H	hub radius
R_T	tip radius
R_Ω	frequency ratio
s	entropy per unit mass
t	time
T	temperature
$\vec{w}$	relative velocity vector

Greek letters

γ	ratio of specific heats
ρ	density
Φ	passage sector angle
$\vec{\omega}_R$	relative vorticity vector
Ω	rotational speed
$\otimes$	dyadic vector product

Subscripts

C	centre of rotation
L	left side (high pressure) of diaphragm in shock tube flow

R	right side (low pressure) of diaphragm in shock tube flow
Ω	axis of rotation
0	equilibrium state for initial conditions
∞	uniform reference state, defined in text

REFERENCES

1. R. P. Shreeve and A. Mathur (eds), *Proc. 1985 ONR/NAVAIR Wave Rotor Research and Technology Workshop, NPS-67-85-008.2*, 1985.
2. I. I. Glass and G. W. Patterson, 'A theoretical and experimental study of shock tube flow', *J. Aeronaut. Sci.*, **22**, 73–101 (1955).
3. M. H. Vavra, *Aero-Thermodynamics and Flow in Turbomachines*, Wiley, New York, 1960.
4. W. D. Hayes, 'The vorticity jump across a gasdynamic discontinuity', *J. Fluid Mech.*, **2**, 595–600 (1957).
5. J. B. Serrin, 'Mathematical principles of classical fluid mechanics', in S. Flugge (ed.), *Encyclopedia of Physics*, Vol. VIII/1, Springer, New York, 19xx, pp. 125–263.
6. R. V. Chima and J. W. Yokota, 'Numerical analysis of three-dimensional viscous internal flows', *AIAA J.*, **28**, 798–806 (1990).
7. E. Dresselhaus and M. Tabor, 'The kinematics of stretching and alignment of material elements in general flow fields', *J. Fluid Mech.*, **236**, 415–444 (1991).